Department of Physics and Astronomy
University of Heidelberg

Bachelor Thesis in Physics
submitted by

Sophia Milanov

born in Düsseldorf (Germany)

2016

Hunting for intermediate-mass black holes: exploring the action-based approach

This Bachelor Thesis has been carried out by Sophia Milanov at the
Max Planck Institute for Astronomy in Heidelberg
under the supervision of
Dr. Glenn van de Ven

Abstract

Hello, here is some text without a meaning. This text should show what a printed text will look like at this place. If you read this text, you will get no information. Really? Is there no information? Is there a difference between this text and some nonsense like “Huardest gefburn”? Kjift – not at all! A blind text like this gives you information about the selected font, how the letters are written and an impression of the look. This text should contain all letters of the alphabet and it should be written in of the original language. There is no need for special content, but the length of words should match the language.

Contents

1 Introduction

Globular clusters (GCs) are self-gravitating, gas-free systems of 10^5 to 10^7 stars which are spherically grouped. There are about 150 of them in the Milky Way (MW) (Harris, 1996). Since they are some of the oldest stellar populations in the universe (approximately 13 Gyr), they contain much information about the assembly history and evolution of the MW. Formerly seen as very simple spherical and isotropic stellar systems with only one stellar population (Meylan and Heggie, 1997), recent research revealed a much higher degree of complexity (that differ in the light-elements abundances (Piotto *et al.*, 2015)). GCs are now known to host multiple stellar populations that challenge our understanding of their formation. Moreover, GCs now also appear dynamically complex, presenting deviations from spherical symmetry, anisotropy in velocity space and significant internal rotation (Zocchi *et al.*, 2012; Bianchini *et al.*, 2013; Kacharov *et al.*, 2014).

Recent attention has been devoted to the search of intermediate mass black holes (IMBHs) in the centre of GCs. These elusive black holes $10^3\,M_\odot < M_\bullet < 10^4\,M_\odot$ could be the missing link between stellar mass black holes ($M_\bullet < 100\,M_\odot$) and super massive black holes (SMBHs, $M_\bullet > 10^5\,M_\odot$) (all black hole masses taken from Carroll and Ostlie (2006, p.639))as they could represent the seed for the formation of SMBHs. Their search in the centre of GCs has partially been motivated by the extrapolation of the $M_\bullet - \sigma$-relation for galaxies (Ferrarese and Merritt, 2000), describing the relation between the mass of a central massive black hole and the velocity dispersion of its host galaxy.

The hunt of IMBHs in Galactic GCs has been primarily based on two methods: 1) detection of radio and X-ray emission due to the accretion of gas in the black hole (Miller and Hamilton, 2002; Maccarone and Servillat, 2008; Kirsten and Vlemmings, 2012; Strader *et al.*, 2012); 2) detection of kinematic signatures in the central region of a GC (Bahcall and Wolf, 1976; Lützgendorf *et al.*, 2013). The first method proved to be difficult because the feeding of a black hole with gas is highly inefficient in a gas poor environment of Galactic GCs.

The kinematic detection of IMBHs is usually based on the analysis of the velocity-dispersion profile in the inner few arcseconds around the crowded centre of a GC in search for a rise of the dispersion. This requires a combination of high angular resolution and high spectral resolving power. For this reason the detection of IMBHs remains still highly controversial.

Currently there are two different kinematic methods trying to detect IMBHs: resolved kinematics & unresolved integrated light (see, for example Bianchini *et al.* 2015). These

methods often deliver significant different results when applied to the same GC. As an

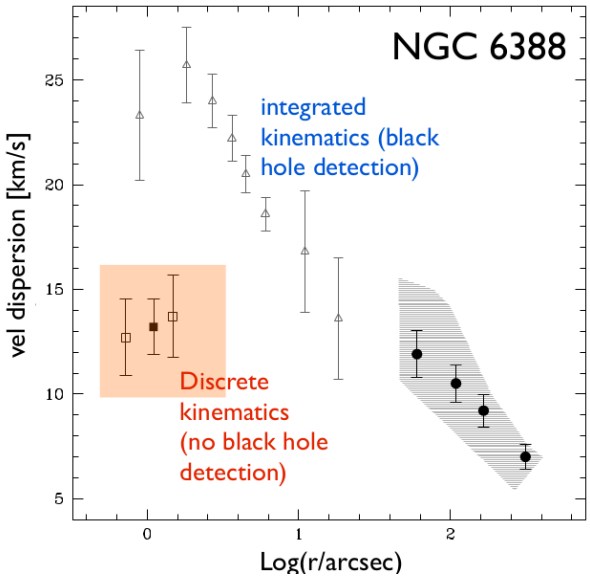

Figure 1: Velocity profile of NGC 6388 derived by the two different methods. We see a cusp given by the integrated kinematics method while there is no cusp with discrete kinematics. Figure adapted from Lanzoni *et al.* (2013) .

example in figure 1 there are the unresolved/integrated IFU kinematics which result in a signature of an IMBH for NGC 6388 (cusp in the velocity dispersion profile) (Lützgendorf *et al.*, 2011) and resolved/discrete kinematics which do not yield IMBHs (no cusp in the velocity dispersion profile)(Lanzoni *et al.*, 2013).

The first detected IMBH of a GC using the IFU method was found in ω centauri (Noyola *et al.*, 2008) observing a rising velocity profile. Two years later, van der Marel and Anderson (2010) used proper motion and a different photometric centre and they could not detect the IMBH. From that there were many investigations in that GC with contradictory results. Using the method of detection of X-ray emission there was no IMBH found (Lützgendorf *et al.*, 2015).

Given these controversial results that prevent us from drawing definite conclusions on the existence of IMBHs in Galactic GCs we propose to introduce a new approach to analyse the effects of an IMBH to the central kinematic of a GC. Our method consists in going beyond the traditional phase space analysis (i.e., analysis of velocity dispersion profiles), by investigating the orbit distribution functions (DFs) of GC stars. Our expectation is that an IMBH could alter the orbital properties of the stars that more closely interact with it.

An orbit is the path an unperturbed, collisionless tracer particle (e.g. a star) will move along in a gravitational potential. Orbits contain information about the gravitational potential generated by the mass distribution of a system in their position and velocity coordinates following Newtons 2nd law. Orbit DFs describe which orbits are populated by how many tracers. From the orbit distribution function together with the overall potential we can draw inferences about the structure and evolution history of the system.

Observations of orbits enabled discoveries or confirmed them:

- From rotation curves of galaxies we see that stars move faster than what expected by the presence of only the mass of luminous matter. There has to be more matter interacting via gravitational forces. This has led to the theory of dark matter (Rubin *et al.*, 1980).
- The orbit of Mercury differs hugely from its calculated Kepler orbit. This is because of its migrating pericentre. Due to the proximity to the sun gravitational forces are so strong that we need to apply general relativity.
- The SMBH Sagittarius A* with a mass of $3.7 \pm 0.2 \times 10^6\,\mathrm{M}_\odot$ was detected by observations of the orbits around the black hole and resulting mass calculations. (Carroll and Ostlie, 2006, p.928)

The investigation of orbit DFs proves to be a powerful tool to understand and model dynamical systems. Orbit DFs are for example widely used to describe or MW galaxy where stars of different components (thin disc, thick disc, bulge, halo) are on different orbits (dynamical distinct) and have different metallicities (chemical distinct).

Describing orbits with the coordinates $(\vec{\mathrm{x}}(\mathrm{t}), \vec{\mathrm{v}}(\mathrm{t}))$ is very difficult since they have a complicated time evolution in 6 coordinates. A better way to describe orbits are integrals of motion. They are constant along the orbit. The classical integrals of motion of a spherical system are energy and angular momentum. But in general the best choice of values to describe an orbit are actions which are as well integrals of motion. One of their advantages is that we can connect them with angle coordinates. They form together a set of canonical conjugate coordinates. Another advantage is that they have an intuitive explanation in contrary to the energy: they quantify the oscillation of the orbit in the different directions of the coordinates. That is why actions are excellent orbit labels and therefore ideal parameters for orbit DFs. Our goal is a description of DFs of GCs and due to above mentioned reasons we investigate in action space.

In this thesis we wish to test the feasibility of the analysis of the action/orbit space in GCs and test whether it could be possible to predict signatures of IMBHs. This will be done by "translating" the traditional phase-space into orbit space, exploiting the potential and the $\vec{x}$ and $\vec{v}$ vectors. Although this type of information (6-D info) is not currently available for Galactic GCs we are motivated by the growing amount of photometric and kinematic data that are already able to deliver a 5-D info (2D spatial info and 3D kinematic info), in particular the high accuracy Hubble Space Telescope (HST) proper motions (see for example Bellini *et al.* (2014)) and the upcoming GAIA data. We will limit our analysis to GC simulations with and without IMBHs to explore this approach. The thesis is structured in two parts: first we familiarize with a phase space analysis of the simulations and then we focus in how to study the orbits and extract predictions of the presence of an IMBH.

2 Method & Theory

In this chapter we give an overview of the theory and methods which are used throughout the investigations. We begin in section 2.1 with the description of the stellar population of a GC. In 2.2 we then explain the kinematic properties, i.e. velocity dispersion and anisotropy parameter. Still in phase space in section 2.3 we introduce density and different potential models. In the next section 2.4.1 we define orbits and their classical integrals of motion. After explaining the benefit of the effective potential in section 2.4.2 we show how we calculate the actions as best choice of integrals of motions(section 2.4.3). Then we give the numerical way of calculating orbits (section 2.4.4) for which we give some examples in the last part 2.5 of this chapter. If not said else we define all properties as specific ones which means they are given in units of the mass of the star.

2.1 Stellar population in GC

The typical stellar population of a GC can be seen in a color magnitude diagram (CMD). We show in figure 2 an example of a CMD extracted from one of our simulations (SIM 1, described in section 3.1). In this CMD the absolute V-band magnitude is plotted against the B-V color. The color code indicates the mass of the stars. The position of a star in the CMD can be interpreted as its evolution stage. Most of the stars are in the main sequence and they are characterized by hydrogen fusion in their cores. There are two main sequence lines one upon the other. These occur due to binary systems whose flux is given by the sum of the single fluxes of the single components, and therefore appear redder and more luminous. These binary systems represent about 7.5 % of the stars in the GC. The position of the main sequence turn-off depends on the age of the system and therefore can be used as an indicator to determine the age of the cluster. Isochrones are curves of evolutionary stages of stars of a single stellar population (SSP) having the same age and metallicity but different masses. Bluewards of this turn off point, following the trend of main sequence stars, there are so called "blue stragglers" which are remnants of stellar collisions or interacting binaries (Binney and Tremaine, 2008, p.628). Continuing from the turn off point there are the sub giant and the red giant branch consisting of stars still fusing hydrogen but only in a shell surrounding a degenerate helium core. They are inflated with a radius much higher than the main sequence stars but have a much lower surface temperature. On the early asymptotic giant branch following the red giant branch the stars are burning helium in their shells. These are the brightest stars of a GC. On the upper part of the red giant branch lies

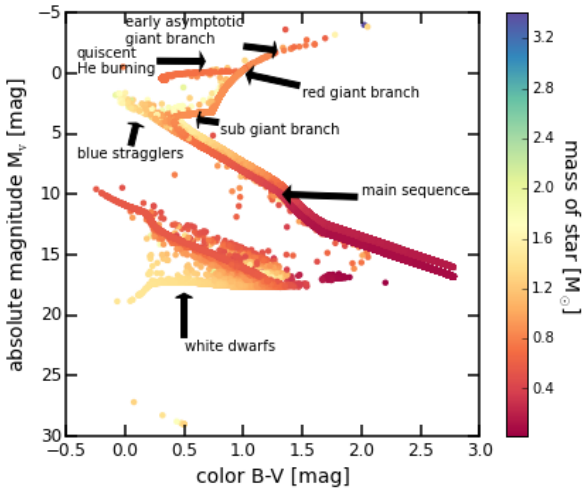

Figure 2: Color magnitude diagram of SIM 1. The absolute V-band magnitude versus the color B-V gives us an overview of the stellar population of this GC. The stars are color coded by their masses. On the main sequence there are two branches. These are caused by binary systems. Following the main sequence there is the turn-off. Going further blue struggles are located. Right to the turn-off there is the sub giant branch followed by the red giant branch. The most luminous stars are situated on the early asymptotic giant branch. At a absolute magnitude of zero there is the horizontal branch where stars burn He quiescently. Below the main sequence and blue stragglers the white dwarfs are located. Having nearly no luminosity dark stellar remnants are situated at the bottom of the CMD.

the horizontal branch. Its stars burn helium in their core and hydrogen in a surrounding shell. In the lower left corner white dwarfs are located. They are stellar remnants which have burnt all of their resources. In a typical GC dark stellar remnants like stellar black holes and neutron stars are present but not visualised in the CMD. In this CMD we see them at the bottom of the figure. (Carroll and Ostlie, 2006, p.476-477).

2.2 Kinematic profiles of globular clusters

We will investigate GCs in phase space by analysing the stellar kinematic profiles (such as velocity dispersion and anisotropy profiles) and the spatial distribution of stars (density profiles and potential).

The stellar velocity dispersion quantifies the spread of different velocities stars at given positions can have. With the actual velocity $\mathrm{v_i}$ of the i-th star, $\langle \mathrm{v} \rangle$ specifying the mean of the velocities of all considered N stars and the mean of the n-th power of the total velocity given by

$$\langle \mathrm{v^n} \rangle = \frac{1}{\mathrm{N}} \sum_{\mathrm{i}=1}^{\mathrm{N}} \mathrm{v_i^n} \tag{1}$$

we can calculate the velocity dispersion as the standard deviation of the velocity distribution:

$$\sigma_\mathrm{i}(\mathrm{r}) \equiv \sqrt{\langle (\mathrm{v_i(r)} - \langle \mathrm{v_i(r)} \rangle)^2 \rangle} = \sqrt{\langle \mathrm{v_i(r)}^2 \rangle - \langle \mathrm{v_i(r)} \rangle^2} \qquad \mathrm{i} = \mathrm{r}, \theta, \phi. \tag{2}$$

For a spherical system it is best to calculate them in spherical coordinates r, θ, ϕ respectively $\mathrm{v_r}, \mathrm{v}_\theta, \mathrm{v}_\phi$. If the GC contains an IMBH the velocity dispersion towards the centre is expected to increase.

The direction of the motion of a star can be described by its anisotropy. In a spherical system we compare the motion in radial direction to the motion in sperical shells at the given distance of the star. The dispersions of motions are described by equation 2. To quantify the anisotropy of the system we use the anisotropy parameter β

$$\beta(\mathrm{r}) \equiv 1 - \frac{\sigma_\theta^2(\mathrm{r}) + \sigma_\phi^2(\mathrm{r})}{2\sigma_\mathrm{r}^2(\mathrm{r})} \tag{3}$$

taken from Binney and Tremaine (2008, eq. 4.61). There the numerator describes the dispersion of motions on the spherical shell while the denominator is given by the squared radial dispersion. If β is positive the anisotropy is radial i.e. the velocity dispersion is larger in radial direction than in tangential direction, if it is negative the anisotropy is

tangential and if $\beta \approx 0$ then the system is isotropic that means the stars have random motions in all directions at the same rate.

2.3 Density & potential

2.3.1 Density of a collisionless stellar system

We calculate the mass density of the GCs by binning the masses on logarithmic equally distributed shells

$$\rho(\mathrm{r}) = \frac{\sum_{\mathrm{r}=\mathrm{r_{in}}}^{\mathrm{r_{out}}} \mathrm{M(r)}}{\mathrm{V(r_{out} - r_{in})}} = \frac{3}{4\pi} \frac{\sum_{\mathrm{r}=\mathrm{r_{in}}}^{\mathrm{r_{out}}} \mathrm{M(r)}}{\mathrm{r_{out}^3 - r_{in}^3}} \tag{4}$$

with the sum of masses of stars with mass M(r) over a volume V which is taken from the radius of the inner shell $\mathrm{r_{in}}$ and the radius of the outer shell $\mathrm{r_{out}}$.

We consider GCs as quasi-collisional stellar system but can approximate them as collisionless motivated by the fact that the dynamical time of a cluster is always shorter than the relaxation time $\mathrm{T_{dyn}} < \mathrm{T_{relax}} < \mathrm{T_{ageGC}} \equiv \mathrm{T_{Hubble}}$. $\mathrm{T_{dyn}}$ is the time of a star to go from one side of the cluster to the other. This takes approximately 10^5 yr. The relaxation time is the time needed to redistribute energies of the stellar encounters and takes about 10^7 - 10^9 yr. The age of the GCs is approximately the Hubble time which is the age of the universe (10^{10} yr). The first term motivates the collisionless approximation while the part starting with $\mathrm{T_{relax}}$ is telling us that a GC has lived for several relaxation times, therefore two-body interaction had time to act. That means in the long term that the system is collisional.

2.3.2 Generating the potential from Poisson's equation

If the system is spherical symmetric the potential and force depend only on the distance from the centre r. Under the condition that the system is collisionless the potential Φ can be derived from the Poisson's equation

$$\Delta\Phi(\mathrm{r}) = 4\pi \mathrm{G}\rho(\mathrm{r}) \tag{5}$$

with the gravitational constant $\mathrm{G} = 6.674 \cdot 10^{-11}\ \mathrm{m^3/kg\ s^2}$ (Mohr *et al.*, 2015) and the density ρ depending only on the distance as well. In general one can use the Poisson's equation for every system but then it is depending on the position vector $\vec{\mathrm{x}}$.

Due to the spherical symmetry the potential can be calculated by

$$\Phi(\mathrm{r}) = -\frac{\mathrm{G}}{\mathrm{r}} \int_0^{\mathrm{r}} \mathrm{dM}(\mathrm{r}') - \mathrm{G} \int_{\mathrm{r}}^{\infty} \frac{\mathrm{dM}(\mathrm{r}')}{\mathrm{r}'} = -4\pi\mathrm{G} \left[\frac{1}{\mathrm{r}} \int_0^{\mathrm{r}} \mathrm{dr}'\mathrm{r}'^2 \rho(\mathrm{r}') + \int_{\mathrm{r}}^{\infty} \mathrm{dr}'\mathrm{r}'\rho(\mathrm{r}') \right] \quad (6)$$

with dM describing the mass of spherical shells as proved by Binney and Tremaine (2008, eq. 2.28).

2.3.3 Other potential models

One of the most simple potentials is the Kepler potential. It describes the potential given by a point mass M

$$\Phi(\mathrm{r}) = -\frac{\mathrm{GM}}{\mathrm{r}} \quad (7)$$

taken from Binney and Tremaine (2008, eq. 2.34). The potential generated by the IMBHs can be described as Keplerian.

Another description of spherical systems is given by the Plummer model. It is based on the assumption that the density is nearly constant in the centre and equals zero at large radii. The given potential is

$$\Phi(\mathrm{r}) = -\frac{\mathrm{GM}}{\sqrt{\mathrm{r}^2 + \mathrm{b}^2}} \quad (8)$$

(Binney and Tremaine, 2008, eq. 2.44a) where M is the total mass of the system and b is the Plummer scale length. In Plummer (1911) Plummer used this potential to describe observations of GCs. the corresponding density to this model is given by Binney and Tremaine (2008, eq. 2.44b)

$$\rho(\mathrm{r}) = \frac{3\mathrm{M}}{4\pi\mathrm{b}^3} \left(1 + \frac{\mathrm{r}^2}{\mathrm{b}^2} \right)^{-\frac{5}{2}}. \quad (9)$$

This model cannot be used to describe the position of a star on its orbit in elementary functions.

In Binney (2014) he claims that GCs can be described by an isochrone (see section 2.1) potential

$$\Phi(\mathrm{r}) = -\frac{\mathrm{GM}}{\mathrm{b} + \sqrt{\mathrm{b}^2 + \mathrm{r}^2}} \quad (10)$$

(Binney and Tremaine, 2008, eq. 2.47). This model delivers analytical functions for the properties of orbits.

2.4 Orbits & integrals of motion

2.4.1 Classical integrals of motion in spherical potential

If a tracer particle, e.g. a star, moves freely in a gravitational potential generated by a mass distribution its path in 6D position-velocity space $(\vec{x}(t), \vec{v}(t))$ is called "orbit". How positions and velocities along the orbit are linked contains information about the potential. With Newton's 2nd law we get the connection between potential $\Phi(\vec{x})$and acceleration $\vec{a}(\vec{x})$ which the star of mass m experiences which is

$$\vec{F}(\vec{x}) = -\nabla\Phi(\vec{x}) = m \cdot \vec{a}(\vec{x}). \tag{11}$$

Here $\vec{F}$ is the force at given position $\vec{x}$.

Despite the description of orbits in the 6D position velocity space it can be described by integrals of motion which are constant along an unperturbed orbit. A spherical potential allows four conserved quantities, i.e. the classical integrals of motions, which are the energy and the three components of the angular momentum. That restricts the orbits in spherical potentials to happen in a plane. The energy is given by the sum of the kinetic energies in the 3D velocity space and the potential:

$$E(r) = \frac{v_x(r)^2 + v_y(r)^2 + v_z(r)^2}{2} + \Phi(r). \tag{12}$$

The total angular momentum

$$\vec{L} = \vec{x} \times \vec{v} = \sqrt{L_x^2 + L_y^2 + L_z^2} \tag{13}$$

can be written as superposition of the angular momenta in each direction which are given by

$$L_k = \varepsilon_{klm} x_l v_m \tag{14}$$

where ε_{klm} is the Levi-Civita symbol.

On a perturbed orbit, e.g. numerical fluctuations near the IMBH, integrals of motion can vary and evolve a time dependency. We assume that the stars move along unperturbed orbits.

2.4.2 The effective potential

The effective potential $\Phi_L(r)$ (see figure 3) describes the potential a star with given angular momentum L experiences in a gravitational potential $\Phi(r)$:

$$\Phi_L(r) = \Phi(r) + \frac{L^2}{2r^2}. \tag{15}$$

which is dependent on the Centrifugal potential $L^2/2r^2$ (taken from Bartelmann (2008, p. 59, eq. 6.27)). The Centrifugal potential describes the energy of the star which it obtains due to its rotation. If the orbit is unbound the effective potential is positive. A

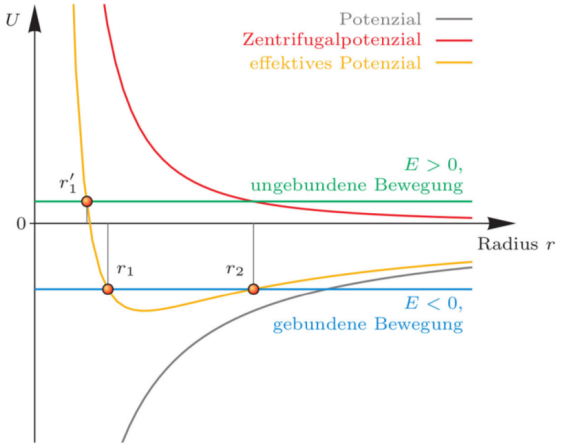

(a) General potential of a central field. The black line is the potential which is the difference between the effective potential (yellow line) and the centrifugal potential (red line). If the effective potential is positive the object is unbound while having a negative potential the object moves on a bound orbit. The points where the effective potential equals the total energy are the peri- and apocentre (r_1 and r_2) of the orbit. The point with the lowest effective potential is the guiding star radius. This is the distance a star with given angular momentum would have on a circular orbit. (Bartelmann, 2008, p.59)

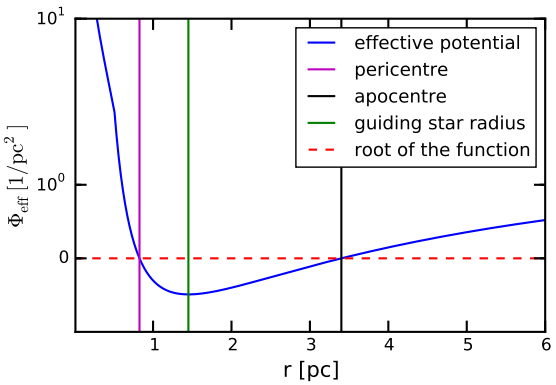

(b) Determination of pericentre, apocentre and guiding star radius given by equation (16). The intersections of zero and effective potential are the peri- and the apocentre of the star (magenta and black lines) and the minimum of the effective potential (green line) is the guiding star radius .

Figure 3: Effective potential (panel a) and its form to calculate pericentre, apocentre and guiding star radius (panel b).

star on a bound orbit experiences negative effective potential.

The radii where the bound orbit has the smallest respectively the highest distance to its gravitational centre are called pericentre r_{min} and apocentre r_{max}. There the effective potential equals the total energy E since the stars do not have any kinetic energy in radial direction there. That results in following function (see figure 3b) which is to solve:

$$\Phi(r_0) - E + \frac{L^2}{2r_0^2} = 0 \Rightarrow \left(\frac{1}{r_0}\right)^2 + \frac{2 \cdot (\Phi(r_0) - E)}{L^2} = 0. \tag{16}$$

r_0 is the solution for peri- and apocentre.

The guiding star radius is the distance at which a star with given total angular momentum would have a circular orbit. This is at the minimum of the effective potential. To get r_g we have to solve

$$\frac{\partial \Phi_L}{\partial r} = \frac{\partial \Phi}{\partial r} - \frac{L^2}{r^3} = 0 \Rightarrow r\sqrt{r\frac{\partial \Phi}{\partial r}} - |L| = 0 \tag{17}$$

where $\sqrt{r\frac{\partial \Phi}{\partial r}} = v_{circ}(r)$ is the circular velocity. The guiding-star distance is an estimation for the radius where the star is on average. Therefore it can be used to have a better comparison of the positions of the stars in the different simulations since in the snapshots the stars are at a random position on their orbit.

2.4.3 Actions

In section 2.4.1 we introduced the classical integrals of motion. Now we introduce actions which are the best choice of values to describe orbits. Like the classical integrals of motion they are constant over time and orbit. We can combine actions with angle coordinates. The angle coordinates are the counterparts to the spatial coordinated while actions work as their momentum. Actions and angles are canonical conjugate coordinates to one another. That means the transformation from phase space to action space is simple and complete. Another reason to have them as best choice is their intuitive physical meaning. They quantify the amount of oscillation along an orbit in i-direction. Generally they can be calculated by

$$J_i \equiv \frac{1}{2\pi} \oint_{orbit} p_i \cdot dq_i \tag{18}$$

with the spatial coordinate in i-direction q_i and the corresponding canonical conjugate momentum p_i.

For most potentials actions cannot be defined analytically but spherically symmetric

potential can be described by relatively straightforward functions. The azimuthal action J_ϕ and the latitudinal action J_θ can be evaluated simply. To calculate the radial action J_r we have to solve an integral numerically. Actions of a spherical potential are found to be

$$J_\phi = L_z, \tag{19}$$

$$J_\theta = L - |L_z|, \tag{20}$$

$$J_r = \frac{1}{\pi} \int_{r_{min}}^{r_{max}} dr \sqrt{2E - 2\Phi(r) - \frac{L^2}{r^2}} \tag{21}$$

(Binney and Tremaine, 2008, p. 221). The azimuthal action is given by the z-component of the angular momentum which is perpendicular to the plane. The polar action is described by the angular momentum without the component in z-direction that means it is given by the part of the angular momentum lying in the orbital plane. The radial action is depending on pericentre and apocentre of the orbit as well as the potential at its distance, the energy and the angular momentum. If the radial action is large than either the orbit is very eccentric and therefore $r_{max} >> r_{min}$ or it has a large radial velocity on a random orbit since the integrand equals the radial velocity which is explained right now.

We give an heuristic explanation of the formula of the radial action. In the general equation to calculate actions, equation (18), we can assume that the corresponding momentum is proportional to the velocity in radial direction, v_r , and that the spatial coordinate is pointing in r-direction and therefore $x_r = r$. We can separate the spherical potential and therefore the motion in r,θ,ϕ-direction. That allows us to split the integral into two integrals, both evaluating the orbit from peri- to apocentre since the orbit is a closed curve which leads us to

$$J_r = \frac{2}{2\pi} \int_{r_{min}}^{r_{max}} v_r(r) dr. \tag{22}$$

Now we consider the motion in plane. We can superpose it into the radial motion with given radius r and corresponding velocity v_r and into tangential motion with given angle ϑ and velocity v_ϑ. The kinetic energy can then be described as the sum of kinetic energy

in radial direction $\mathrm{E_r}$ and in angular direction E_ϑ which is the rotation energy:

$$\mathrm{E_{kin}} = \mathrm{E_r} + \mathrm{E}_\theta, \tag{23}$$

$$\mathrm{E_r} \propto \frac{\mathrm{v_r^2}}{2}, \tag{24}$$

$$\mathrm{E}_\vartheta \propto \frac{\mathrm{v}_\vartheta^2}{2} \propto \frac{\mathrm{L}^2}{2\mathrm{r}^2}. \tag{25}$$

We can write the radial energy as sum of the other energies and derive the radial velocity from that:

$$\begin{aligned}
\mathrm{E_r} &\propto \mathrm{E_{tot}} - \mathrm{E_{pot}} - \mathrm{E}_\vartheta, \\
&\propto \mathrm{E} - \Phi(\mathrm{r}) - \frac{\mathrm{L}^2}{2\mathrm{r}^2} \\
\Leftrightarrow \frac{\mathrm{v_r^2}}{2} &\propto \mathrm{E} - \Phi(\mathrm{r}) - \frac{\mathrm{L}^2}{2\mathrm{r}^2} \\
\Longrightarrow \mathrm{v_r} &\propto \sqrt{2\mathrm{E} - 2\Phi(\mathrm{r}) - \frac{\mathrm{L}^2}{\mathrm{r}^2}}.
\end{aligned}$$

We can set this result in the integrand of (22) which gives us the equation of the radial action.

2.4.4 Numerical orbit integration

To derive the potential we solve the integrals of the Poisson's equation (6) numerically by using the Gauss-Legendre quadrature

$$\int_a^b f(x)dx \approx \frac{b-a}{2} \sum_{i=1}^{n} w_i f\left(\frac{b-a}{2}x_i + \frac{a+b}{2}\right) \tag{26}$$

where the points $\mathrm{x_i}$ and the weights $\mathrm{w_i}$ are derived from the Legendre polynomials and a and b are the integration limits. This gives us the numerical formula for the potential

$$\begin{aligned}
\Phi(r) = &- 4\pi G \cdot \frac{1}{2} \sum_{i=1}^{n} w_i \left(\frac{r}{2}x_i + \frac{r}{2}\right)^2 \rho\left(\frac{r}{2}x_i + \frac{r}{2}\right) \\
&- 4\pi G \cdot \frac{\infty - r}{2} \sum_{i=1}^{n} w_i \left(\frac{\infty - r}{2}x_i + \frac{\infty + r}{2}\right) \rho\left(\frac{\infty - r}{2}x_i + \frac{\infty + r}{2}\right)
\end{aligned} \tag{27}$$

To describe the orbit we need its position and velocity at each time step we use the numerical leapfrog method which is a second-order accurate, time reversible, sympletic integrator. Second-order accurate means that the error of the position after one timestep Δt is proportional to the 3rd power of the timestep and sympletic means that it conserves the volume of the phase-space. This integrator uses kick steps and drift steps. When doing a kick step the position stays the same and the momentum changes. When doing a drift step the position changes and the momentum stays the same. One variant is the "drift-kick-drift" leapfrog where the steps are calculated as follows:

$$\vec{\mathrm{x}}_{1/2} = \vec{\mathrm{x}} + \frac{1}{2}\vec{\mathrm{v}}\Delta\mathrm{t} \qquad ; \qquad \vec{\mathrm{v}}' = \vec{\mathrm{v}} - \nabla\Phi(\vec{\mathrm{x}}_{1/2})\Delta\mathrm{t} \qquad ; \qquad \vec{\mathrm{x}}' = \vec{\mathrm{x}}_{1/2} + \frac{1}{2}\vec{\mathrm{v}}'\Delta\mathrm{t} \qquad (28)$$

(adapted from Binney and Tremaine (2008, eq. 3.166a)). The second time derivation of $\vec{\mathrm{x}}(\mathrm{t})$ is the acceleration which we can assume as constant for small enough timesteps. Integrating the acceleration gives us the velocity at given time t with constant values for the acceleration and velocity. Another integration leads to the position at time t with constant acceleration, velocity and position: $\vec{\mathrm{x}}(\mathrm{t}) = \frac{1}{2}\vec{\mathrm{a}}_0\mathrm{t}^2 + v_0 t + x_0$. If we disturb this position at time $\mathrm{t_i}$ with the timestep $\Delta\mathrm{t}$ then we get equation (**??**). The derivation of the specific potential can be expressed through equation (11) so that $\nabla\Phi(\vec{\mathrm{x}}) = -\vec{\mathrm{a}}(\vec{\mathrm{x}})$. If the timestep Δ is small enough we can assume that the acceleration is constant for this step and that the acceleration of the half step can be described by the sum of half of the acceleration at the beginning of the step and half of the acceleration at the end of the step. That allows us following substitution: $-\nabla\Phi(\vec{\mathrm{x}}_{i/2}) = \frac{\vec{\mathrm{a}}(\vec{\mathrm{x}}_{i+1})+\vec{\mathrm{a}}(\vec{\mathrm{x}}_i)}{2}$ and leads us to (**??**):

3 Analysis

In this section we analyse different aspects of the simulations. In section 3.1 we describe the simulations, their underlying models and give an overview of their properties. The next step in section 3.2 is to fit isochrones to the CMD to verify given age and metallicity. After that we investigate the phase space in section 3.3. We look for a rise in the velocity dispersions of the GCs with IMBH and examine the anisotropy parameters. Then we determine the density distribution, check the system if we can apply simplifications as sphericity and generate the potential. From that we change into action space in section 3.4. There we apply the radial action over different properties as the guiding star distance or the classical integrals of motion to see if we can find a signature of an IMBH.

3.1 Description of the simulations

We consider a set of Monte Carlo cluster simulations, developed with the Monte Carlo code MOCCA of Hypki and Giersz (2013) (see also Giersz (1998)). The simulations include an initial mass function, stellar evolution, primordial binaries, and a relatively high number of particles, providing a realistic description of the long-term evolution of GCs with a single stellar population.

All the simulation had a metallicity of [Fe/H]=−1.3 and Kroupa (2001) initial mass function. The first simulation (from Giersz *et al.* (2015), kindly shared by the authors) contain an IMBH of $10^4\,M_\odot$ and its initial condition is drawn from a King model with concentration parameter W_0=6, 6.9×10^5 initial number of particles, 95 % of which are binary systems. We consider two snapshots of the simulation, one at 10 and one at 7 Gyr. We call these snapshots SIM1-IMBH and SIM2-IMBH, respectively. The other two simulations (from Downing *et al.* (2010), kindly shared by the authors) do not contain an IMBH and have an initial number of particles of 5×10^5 and 2×10^6, 10 % of initial binaries, and initial conditions drawn from a Plummer (1911) model with a ratio between the initial tidal radius and half-mass radius of 75. We consider a 11 Gyr snapshot for both simulations and we call them SIM3-NOIMBH and SIM4-NOIMBH, respectively.

We summarize in table 1 the properties of the simulations for the time-snapshots considered.

The output of the simulations relevant for our work are for each star: the position vector x, the velocity vector v in Cartesian and polar coordinates, mass, luminosity, magnitude B and V band and whether the star is a binary or not.

Name of the simulation	Number of particles	Total mass [$M_\odot$]	Mass of theIMBH [$M_\odot$]	r_m [pc]	Age [Gyr]	Binary fraction[%]
SIM 1 - IMBH	1026735	3.09×10^5	10102	4.13	10	7.5
SIM 2 - IMBH	1079376	3.26×10^5	8902.3	3.58	7	7.8
SIM 3 - NOIMBH	468627	1.73×10^5	0	7.89	11	3.0
SIM 4 - NOIMBH	1851556	6.70×10^5	0	5.41	11	3.3

Table 1: Overview of the data of the simulations. We show the basic properties of each simulation which are number of particles, the total mass, the mass of the IMBH, the half mass radius, the age and the binary fraction. The half mass radius is defined by the radius which includes half of the mass of the whole system.

We compute the half-mass radius r_m given in table 1 by calculating the distance where half of the mass of the GC is inside the sphere of given distance and half of the mass is distributed outside of this sphere. We need it to compare aspects of the different simulations especially in phase space investigations since their actual distance is depending on the simulation and is therefore not comparable. In action space we use the guiding star radii (see equation (17) in section 2.4.2).
To get familiar with the simulation we first have a look at the spatial distribution of the stars.

3.2 Investigation in color magnitude space

As mentioned in 2.1 the CMD is showing the evolution stage of a star dependent on its position. If one does not know age or metallicity of the system isochrones (taken from Bressan *et al.* (2012)) can be fitted on the CMD. In figure 6 we plot several isochrones (see section 2.1) to our CMD to determine which one fits best. This gives us the age and the metallicity of the system. The age is best determined in the turn off point. We see that the age $10 \pm 0.5\,\mathrm{Gyr}$ is given from the best fitting isochrones. metallicity

The stars in a GC are characterized by different stellar masses as shown from the color-code of figure 6. The evolved stars (red giants, horizontal branch stars, asymptotic giants) are characterized by a mass of $\approx 0.8-0.9\,M_\odot$ while the main sequence stars have masses from $\approx 0.8-0.9\,M_\odot$ (at the turn-off) down to $0.1\,M_\odot$ at the faint end. Having a mass spectrum is important for the long-term dynamical evolution of a GC and gives rise to the phenomena of mass-segregation/energy equipartition.Trenti & van der marel 2013 . Throughout the following investigations we do not consider the mass dependence induced by energy equipartition and do not make a distinction for stars with different

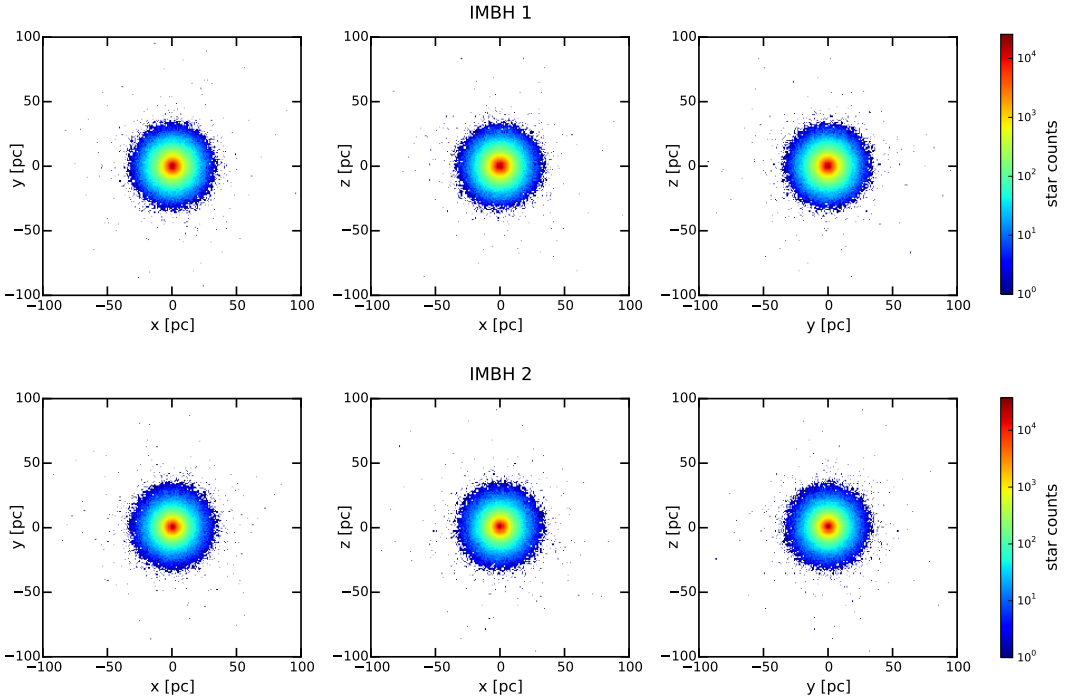

(a) SIM 1 & SIM 2. The GCs are spread until 100 pc with most of the stars located in the inner 40 pc.

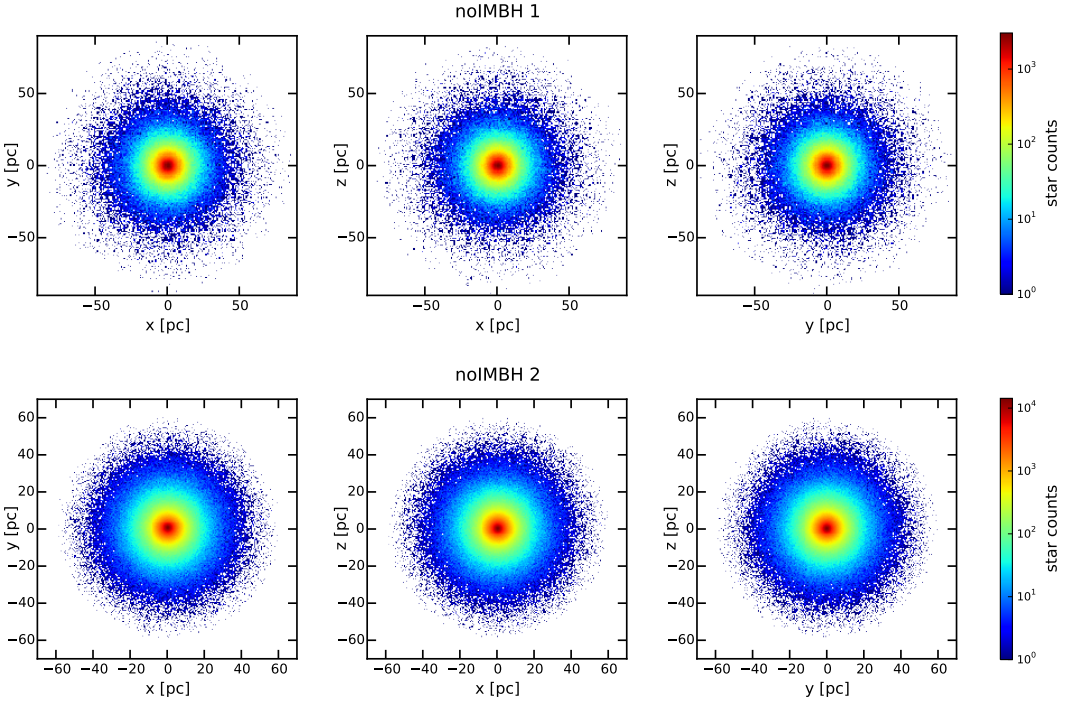

(b) SIM 3 & SIM 4. The GC is spread until 90 pc (SIM3) and until 60 pc (SIM4).

Figure 4: Spatial distribution of stars in the simulated GCs. The stars are distributed spherically with most of the stars in the inner part. The stars of the GCs with IMBH are less spread in the outer parts except very few which are far outside. This is simply due to the different initial concentration conditions of the simulations. In the GCs without IMBH the stars in the outer part are less accumulated but the furthermost stars still in the main sphere.

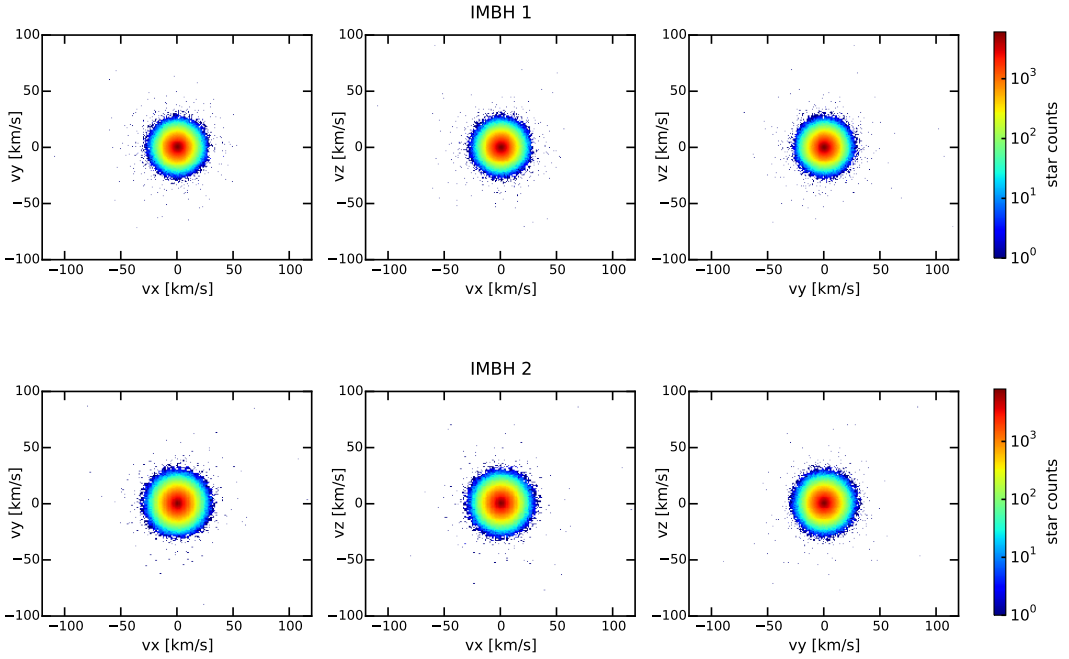

(a) SIM 1 & SIM 2. The stars' velocities are spread until 120 $^{\mathrm{km}}/_{\mathrm{s}}$ with most of them reaching 30 $^{\mathrm{km}}/_{\mathrm{s}}$.

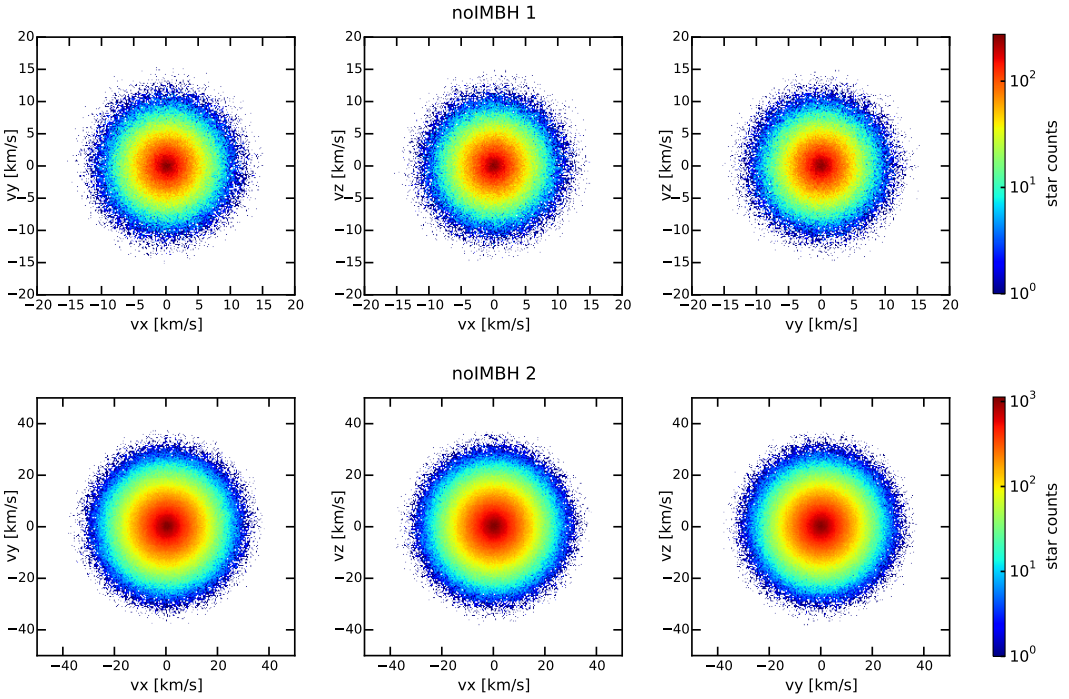

(b) SIM 3 & SIM 4. The stars' velocities are spread until 15 $^{\mathrm{km}}/_{\mathrm{s}}$ for SIM 3 whereas they spread until 40 $^{\mathrm{km}}/_{\mathrm{s}}$ for SIM 4.

Figure 5: Velocity distribution of stars in the simulated GCs. The velocities are isotropically spread around $\vec{v} = 0$. Most of the stars have low or no velocity while a few have high velocities in different directions. There are no overall streaming motions.

masses.

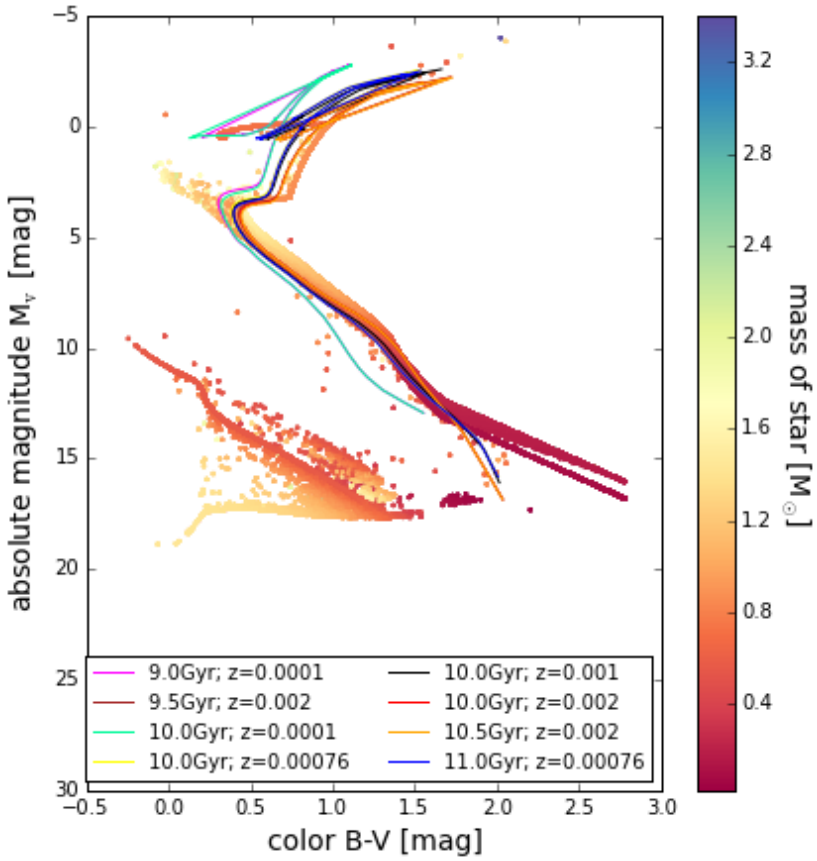

Figure 6: Color magnitude diagram of SIM 1 overplotted with different isochrones. We recognize how we can determine the age based on the turn off point. This verifies the age and the metallicity of this GC of 10 Gyr and 0.001.

3.3 Investigation in phase space

First we investigate the GC in phase space for the set of simulations that we use throughout this work. We start with the velocity dispersion and the anisotropy parameter then wel have a density profile and from that get the potential.

3.3.1 Kinematics

With equation (2) from section 2.2 we can calculate the velocity dispersion in each coordinate direction $\sigma_\mathrm{r}, \sigma_\theta, \sigma_\phi$. For every bin we take the same amount of stars and calculate the dispersion along the radius of the GC. As radial values we use the average radius of the stars falling in the bins. To compare all simulations we plot the dispersion

over the distance in units of the half-mass radius. The half mass radii of the simulations can be taken from table 1. As expected, in figure 7 we see a rise in the centre for the simulations with IMBH. This is due the high gravitational potential of the IMBHs which disturbs the dynamics of close stars. The rise is equally visible in all three velocity components. This is since the kinematics are isotropic in the centre of the GC (see figure 8). There is no difference in the polar (figure 7c) and the azimuthal (figure 7b) velocity dispersion profiles because the system is spherical symmetric. In the outer regions the radial velocity dispersion 7a decreases linear while the tangential slope becomes less steep. The motion in the outer angular shells seems to be different to the motion in radial direction.

In figure 7 we note a difference in the radial and in the tangential velocity dispersion. To properly quantify that difference we consider the anisotropy profile in figure 8. Anisotropy can be calculated from equation (3) given in section 2.2. Radial anisotropy means that there is higher velocity dispersion in radial direction than in angular direction. This comes probably along with a substantial number on eccentric orbits. The profile is binned the same way as the velocity dispersions and given in units of the half-mass radius. In the central $\approx 2\,\mathrm{r_m}$ of all GCs there is nearly the same anisotropy: isotropy in the centre and radial anisotropy while going in the outer parts. That means the systems are radial anisotropic. In the centre the anisotropy is zero. There the system is isotropic and the stars move in no preferred direction. The GCs with IMBH are most radially anisotropic at about 4 half-mass radii. The other GCs are becoming more radial anisotropic the further away from the centre it is. The difference is due to different truncation prescriptions of the simulations.

3.3.2 Spatial distribution

It is important to determine the density distribution for several reasons:

- We want to compare the radial density profiles of the simulated GCs to see if they are similar to each other
- and if they can be described by classical GCs profiles like the Plummer potential (see section 2.3.3).
- Can we maybe already determine a signature of the IMBH in the density distributions?

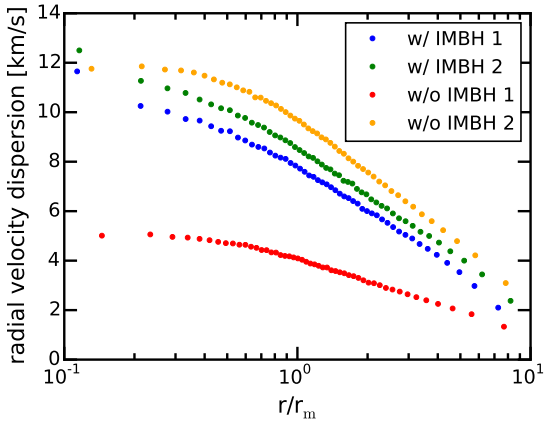

(a) Radial velocity dispersions

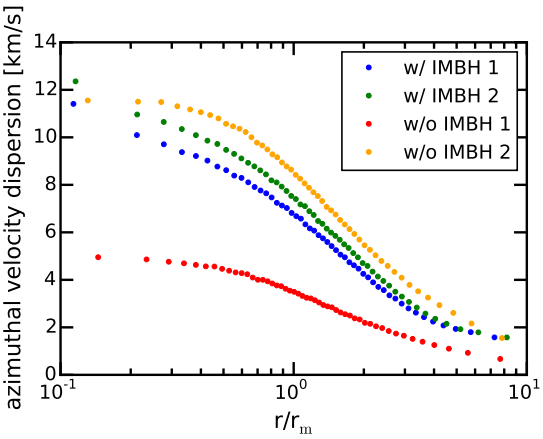

(b) Azimuthal velocity dispersions

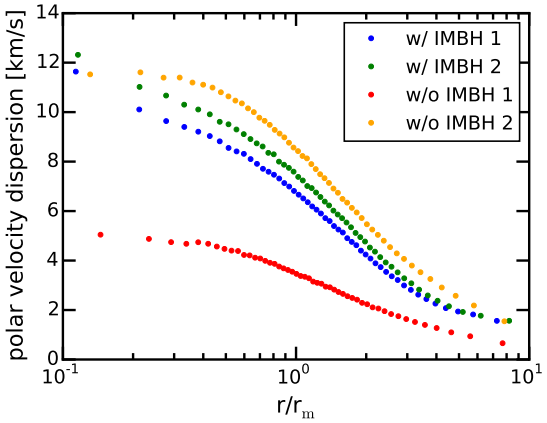

(c) Polar velocity dispersions

Figure 7: Velocity dispersion profiles of v_r, v_ϕ, v_θ as a function of the radius in units of the half-mass radius r_m. Blue and green points are the velocity dispersions of SIM 1 and 2 and the red and yellow ones are the velocity dispersions of SIM 3 and 4. They are binned in a way that each bin contains the same amount of stars. The given radius is the mean radius of the stars of each bin. We can see that the velocity dispersion of the simulations with IMBH rises towards the centre whereas the simulations without IMBH exhibits a cored profile.

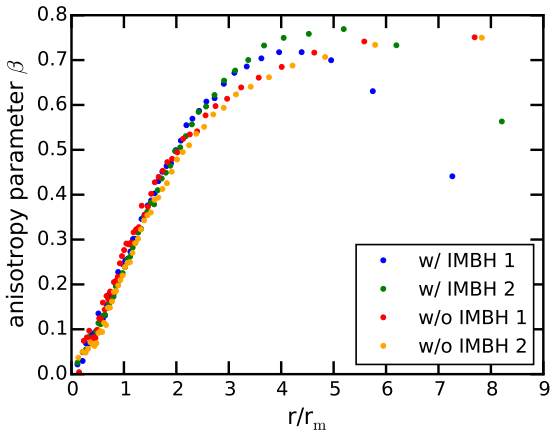

Figure 8: Profile of the anisotropy parameter β (see section 2.2 for definition). The colors are given as in figure 7. All simulations are isotropic in the centre and become increasingly radial anisotropic in the intermediate regions. The simulations with IMBHs have a peak at 4 and 5 half-mass radii where they are most radial anisotropic. Some difference in anisotropy is observable between the simulations with and without IMBH. This is due to different truncation prescriptions used in the simulations. We note that within $\approx 2\,\mathrm{r_m}$ all simulations exhibit the same anisotropy profile.

- As mentioned in section 2.3.2 we need the density profile to generate the overall gravitational potential of the GCs stellar distribution.

The density profile in figure 9 shows the density calculated by equation (4) of the system over its radius. As bins we use radial shells with logarithmic spacing chosen so that there are at least 100 stars per bin to avoid low-number statistic. Outside of the cluster the density is set to 0. In the centre of the GCs (the distance of the 300th star of each simulation) we extrapolate the density profiles by setting it to the constant value of the innermost shell.

We try to find an analytic fitting function to the density profile for. This is essential for then calculating the potential from the Poisson's equation (5) and to carrying out our following analysis. We use two variations of an exponential function which could fit well. Also we want to check if the density follows a classical GC profile which i.e. is the Plummer profile (see equation 9 in section 2.3.3). Figure 9b shows the different analytic fitting functions that we tried on SIM 1. We see that we cannot find a simple fitting function nor a classical profile which describes the density throughout its radial extent. To get a analytical function we will use the interpolated density given in figure 9c.

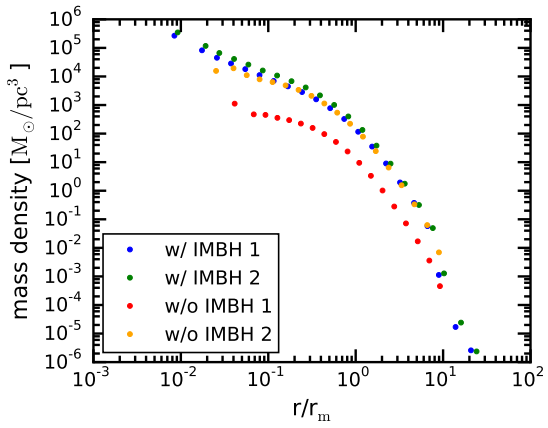

(a) Mass density profiles of all four simulations.

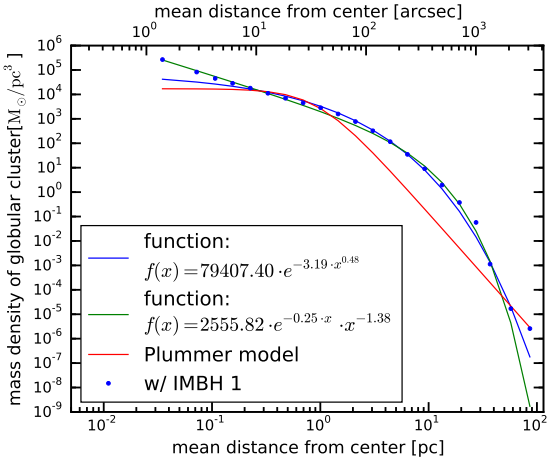

(b) Analytically fitted mass density profile of SIM 1.

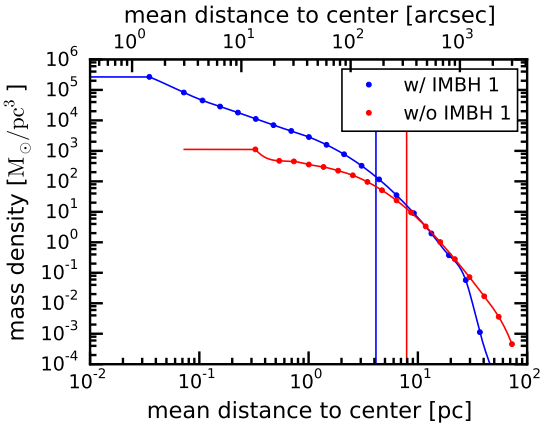

(c) Interpolated mass density profiles of SIM 1 and SIM 3.

Figure 9: Stellar mass density profiles. The density in $M_\odot/pc^2$ is plotted against the radius in units of the half-mass radius in panel a. The density of the GC with IMBH is everywhere larger than the density of the GC without IMBH. In the centre there is a raise in the density of the GC with IMBH whereas the other GC stays approximately on the same level with a cored profile. Both start decreasing at about $0.5\,r_m$. We can see in panel b that it is not simple to find an analytical function describing the density globally for both small and large radii. That is why we interpolate it in panel c. Everything out of the GC is set to zero while the innermost density is set to be the value of the innermost point. The analytical interpolation is needed in the end of this section to calculate the potential given by the density.

We test the sphericity of the GC, its centre of mass (COM) and the mean velocities in polar coordinates. Sphericity allows the usage of analytical methods that are very straight forward, especially for determing the potential of the globular cluster and from that the actions in action space. The centre of mass is being tested to see if we can assume the origin of the coordinate system as centre of the GC or if we have to consider another centre. The mean velocities are tested to see if the GC rotates. Then they would show a substructure. If there is no rotation the mean velocities should distribute around zero. We will test the sphericity and the centre of mass in one step by splitting the GC into octants and compare their mass density profiles. As one can see in figure 10 they are acceptable overlaying. This is done first for the centre of the coordinate system. We do the same for the centre of mass which is calculated by formula insert formula here and compare it in figure 10.

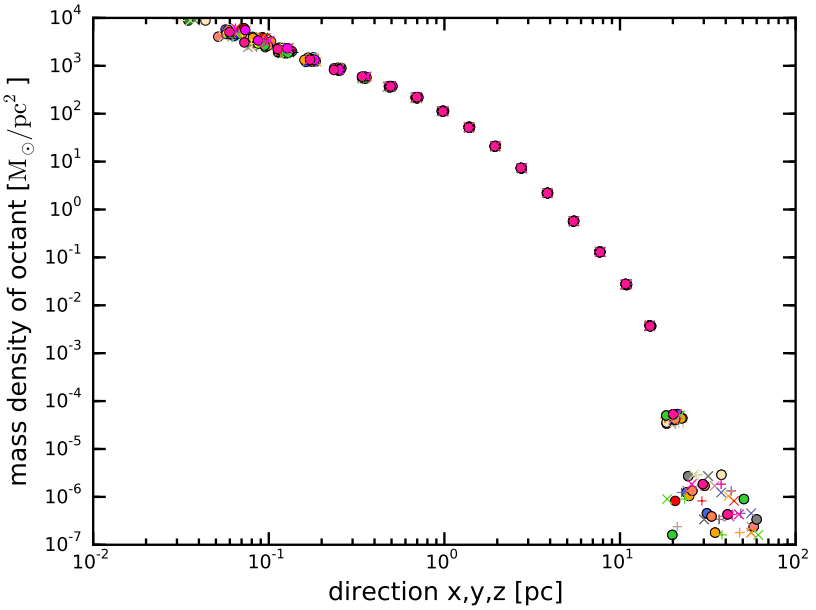

Figure 10: Test for sphericity and center of mass of SIM 1.

From the density profile we can compute the potential using the Poisson equation (**??**) as described in section 2.3. The potential is given by the potential calculated from the mass density of the stars only and, if there is one, the potential of the IMBH is added as a point source Kepler potential (see equation (7) in section 2.3.3).

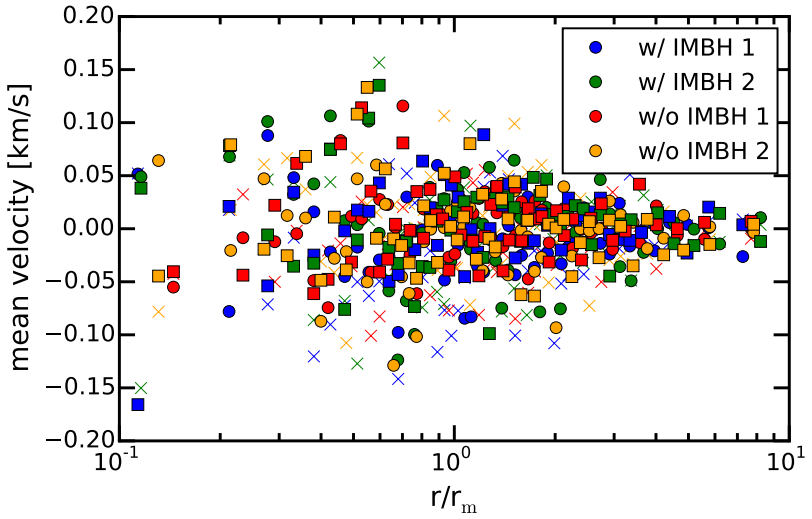

Figure 11: Test for inner rotation in GC of SIM1.

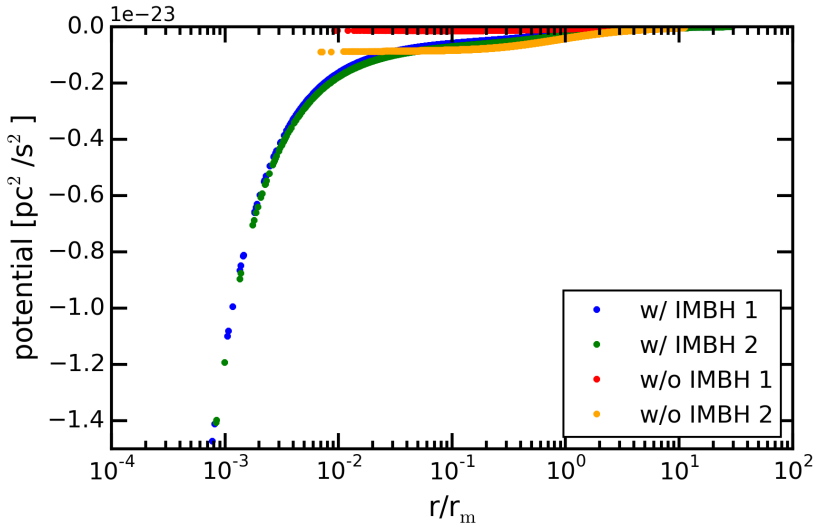

Figure 12: Potential of all GCs. SIM 1 and SIM 2 are nearly overlaying. They are the same simulation at different ages. The simulation lost 5 % of its stars with 10 % of the total mass while the IMBH gained 13 %. The potential of the stars declines while the potential of the IMBH rises so the potential stays the same. The GCs without IMBH remain constant in the inner part (until 0.5 half mass radii) and decrease from the points where their densities decrease.

3.4 Investigations in action space

Now we change our investigations from phase space to action space. We do this by calculating the classical integrals of motions given by equations (14) and (12) (see section 2.4.1) and the actions, especially the radial action given by equations (19) in section 2.4.3. We have a look at the energies and angular momenta of the stars and compare them with the radial actions. Our main goal is to find any systematic signatures for the simulations with IMBHs that can be considered as the direct evidence of the dynamical effect of the IMBH itself. For this reason we investigate selected stars which show an abnormal behaviour in above-mentioned plots and compare them to the rest of the data to see where we find them.

3.4.1 Energy

In figure 13 we plot the radial action versus the energy of the star as histograms for all GCs. We see J_r significantly different than zero. That means we have many stars moving on radial orbits as expected from the radial anisotropy measured in figure 7a in section 3.3.1 We see clearly some stars outside of the moon shape. They have either no radial action and high energy (below $[-4 \times 10^{-24}]\mathrm{pc}^2\mathrm{s}^2$) or nearly no energy and high radial action (above $500\,{}^{\mathrm{pc\ km}}/_{\mathrm{s}}$).

We check the effective potential of the stars of the group to get information of their orbits and their actual positions. In figure 14 show one exemplary graph for each group taken from SIM 1.

The first group of stars of SIM 1 contains 280 of the nearest 768 stars including 85 % of the first 100 stars. Since they have really low (nearly 0) radial actions they are on circular orbits. We can that clearly see in the effective potential in figure 14a. There the peri- and the apocentre are the same which is typical for a circular orbit. The nearest 30 on circular orbits around the IMBH are certainly locked to the IMBH. That is why we do not see this signature for SIM 3 and SIM 4. The other stars of this group are likely to be locked to the IMBH as well while the rest of the near stars which are not in this group seem to be near to or in their pericentre on more eccentric orbits and therefore not locked to the IMBH.

The second group of stars with high radial actions and nearly no energy includes 20 stars and cannot be clearly related to the IMBH. 12 of them are some of the furthermost stars of the snapshot. All these stars are in their apocentre on very eccentric orbits. In figure 14b This eccentricity could be caused by the IMBH but since most of their

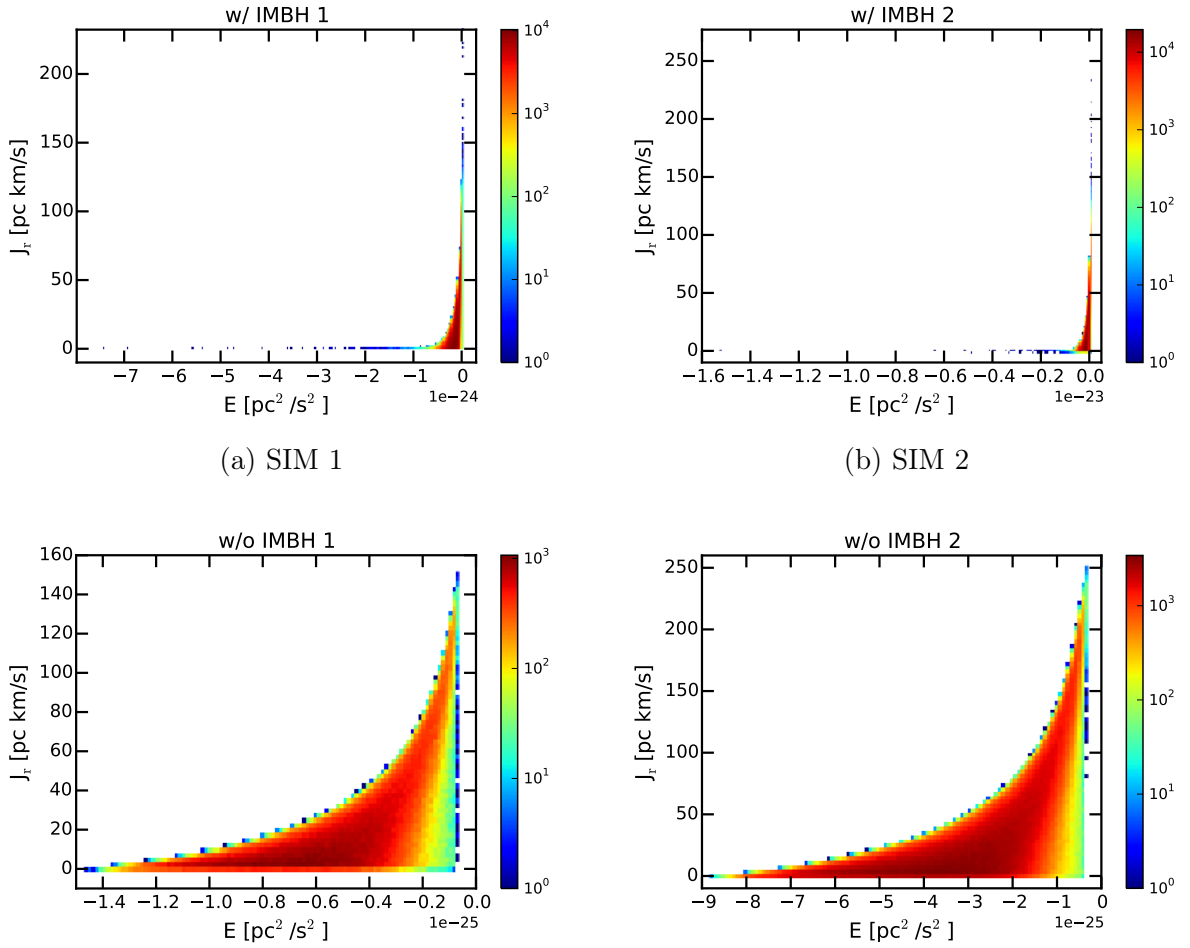

(a) SIM 1

(b) SIM 2

(c) SIM 3

(d) SIM 4

Figure 13: Radial action over energy. In panels a and b it is plotted for both simulations with IMBH and the lower ones are for the simulation without IMBH. We find the crescent shape from panels c and d clearly in panels a and b. But in SIM 1 and SIM 2 there are some stars differing from this shape. Some have high energy with no radial actions (henceforth referred to as group 1) while others have high radial actions with nearly no energy (henceforth group 2).

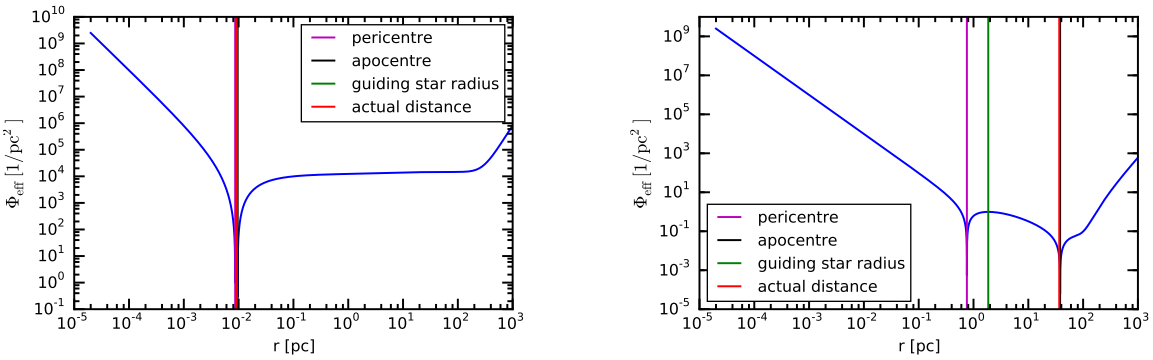

(a) Star of group 1

(b) Star of group 2

Figure 14: Effective potential of exemplary stars of both groups from figure 13. The star of group 1 is clearly one a circular orbit with $r_{min} \approx r_g \approx r \approx r_{max}$. The star of group two has a highly eccentric orbit and its actual position is in its apocentre.

pericentres are at a few pc we cannot assume much interaction with the IMBH for those stars. Another reason that these stars do not occur in this way in SIM 3 and SIM 4 can be due to different truncation prescriptions used in the simulations (see figure 8). These stars are nearly outside of the GCs and have about zero energy so they could have been excluded in SIM 3 and SIM 4.

We might get these high energies from former binaries which were divided earlier in the evolution of the GC. One of the stars could have been captured on a circular orbit near the centre while the other could have been left on an unbound orbit and have left the system. To check this we will plot the same values only for our actual binary systems. As we see in figure 15 the binary systems are behaving like single stars. There is no signature that the divergent stars are leftovers of former binaries.

3.4.2 Angular momentum

Next we plot the radial actions over the absolute angular momenta of the stars of the simulations again as histograms. In figure 16 we can see a triangular shape which seems characteristic. Inside this shape we see some substructure in the GCs with IMBH. The stars outside the shape are the stars of group 2 which we see in figures 13 and 15 as the stars with no energy and high radial actions. Obviously they do not seem to have a specific angular momentum. We do not know how to identify the stars in the substructure. There could be a mass-dependent correlation due to dynamical mass segregation.

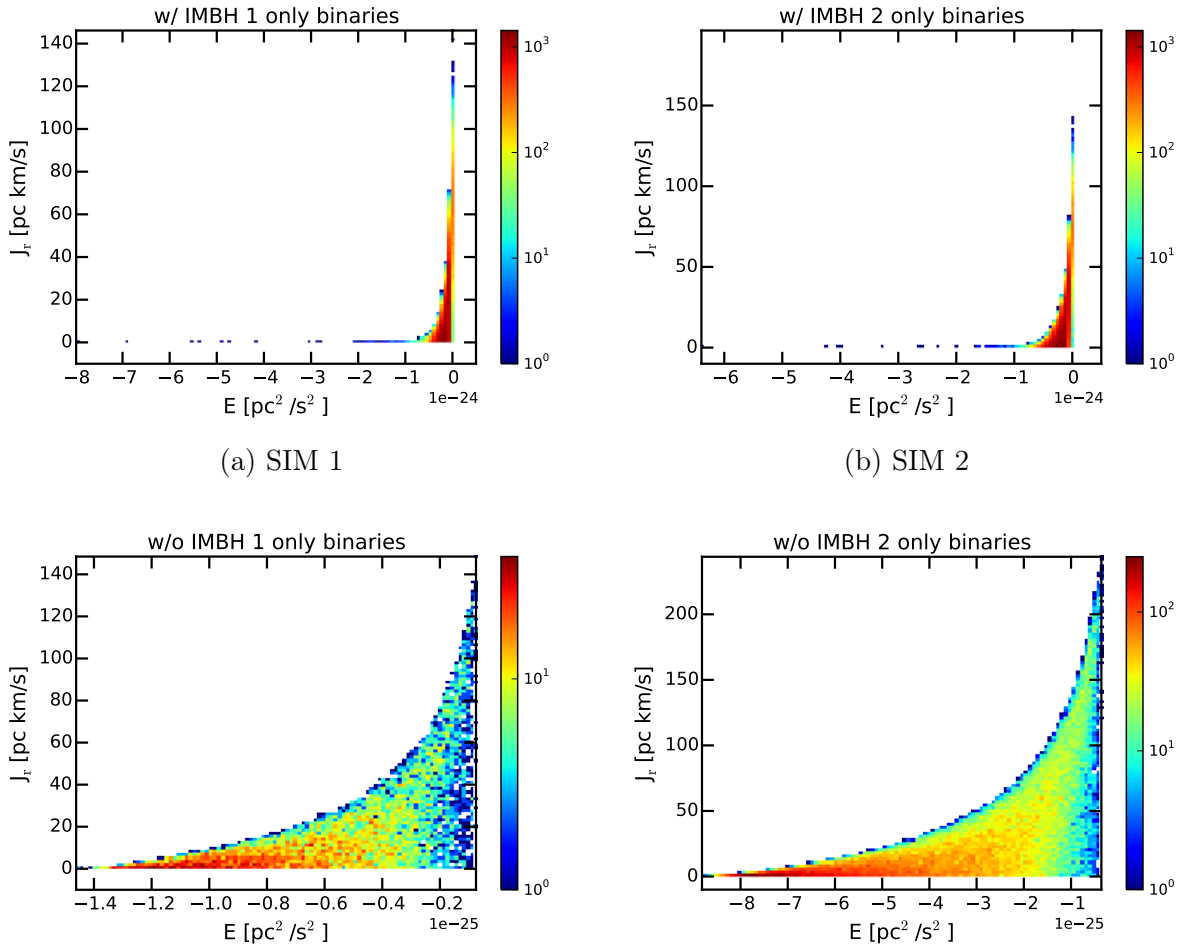

(a) SIM 1

(b) SIM 2

(c) SIM 3

(d) SIM 4

Figure 15: Radial action over energy only of binary systems. We see a similar distribution of stars as in figure 13.

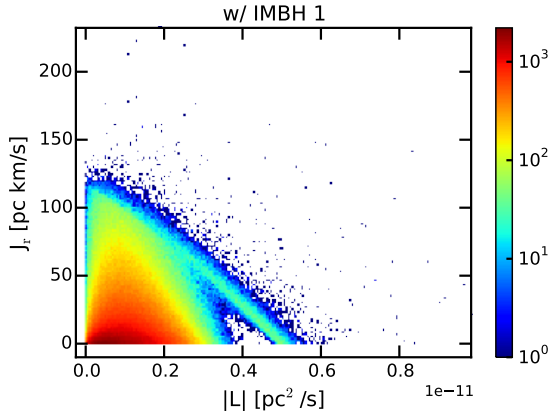

(a) SIM 1

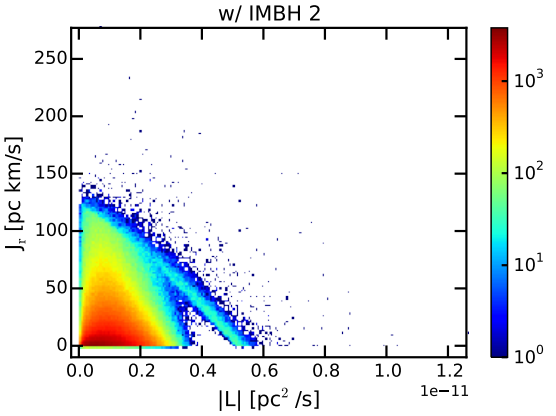

(b) SIM 2

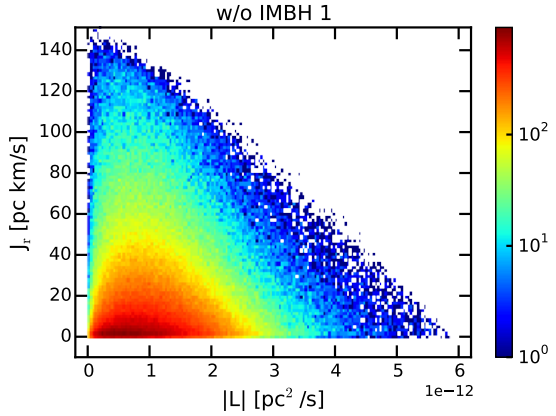

(c) SIM 3

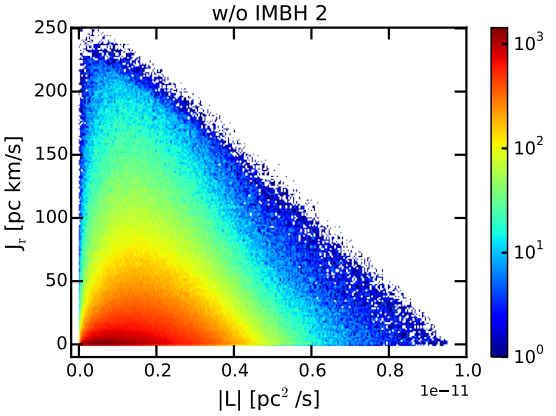

(d) SIM 4

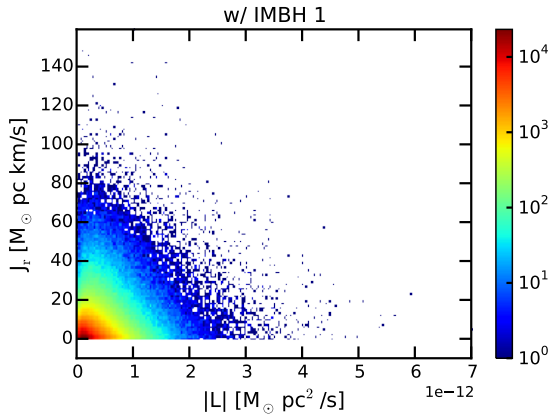

(e) SIM 1 mass weighted

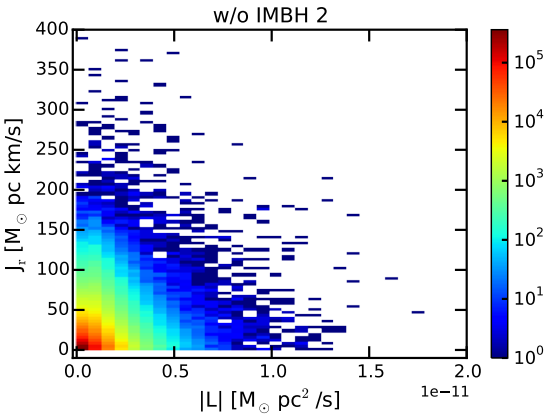

(f) SIM 4 mass weighted

Figure 16: Radial action over angular momentum. Panels c and d look again very similar to each other with no recognizable substructure. In the panels a and b there are stars above the main shape. In the shape we can clearly see a substructure from about 0.3 to about 0.5 pc^2/s in nearly the whole radial action range. In panels 16e and 16f

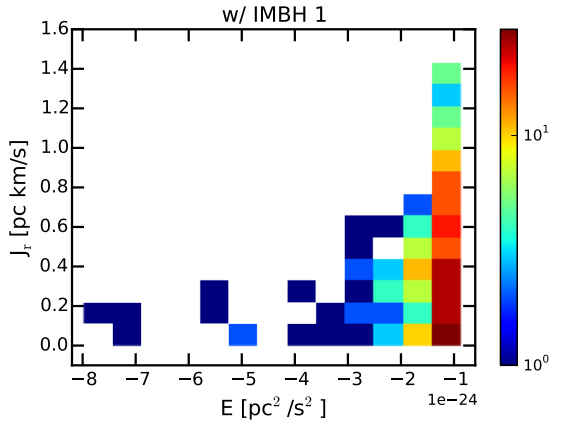

(a) Radial action over energy only for IMBH influenced stars of SIM 1.

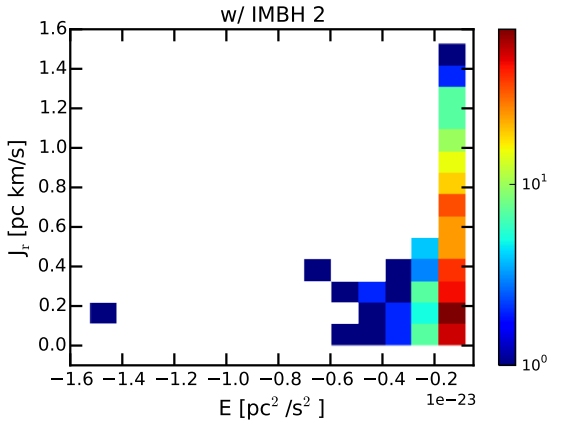

(b) Radial action over energy only for IMBH influenced stars of SIM 2.

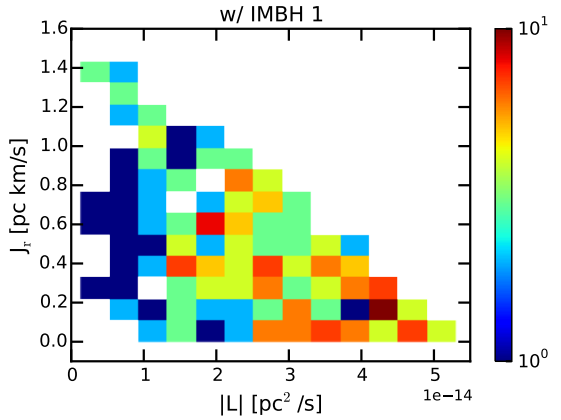

(c) Radial action over angular momentum only for IMBH influenced stars of SIM 1.

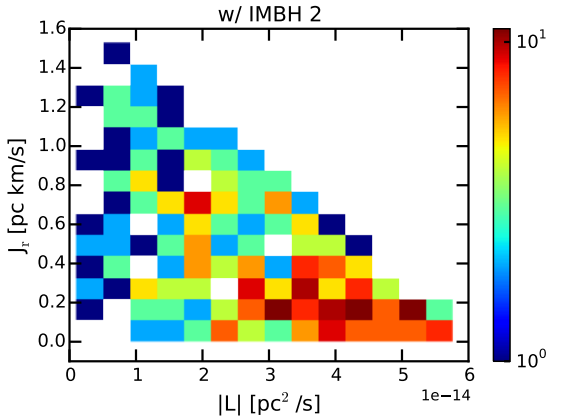

(d) Radial action over angular momentum only for IMBH influenced stars of SIM 2.

Figure 17: Close-up of radial action versus energy and angular momentum for group 1 stars. In the panels
??

3.4.3 Guiding star radius

We extract these divergent stars and determine their properties. First we check the positions of their actions depending on their guiding star radii. In graph 18 the radial

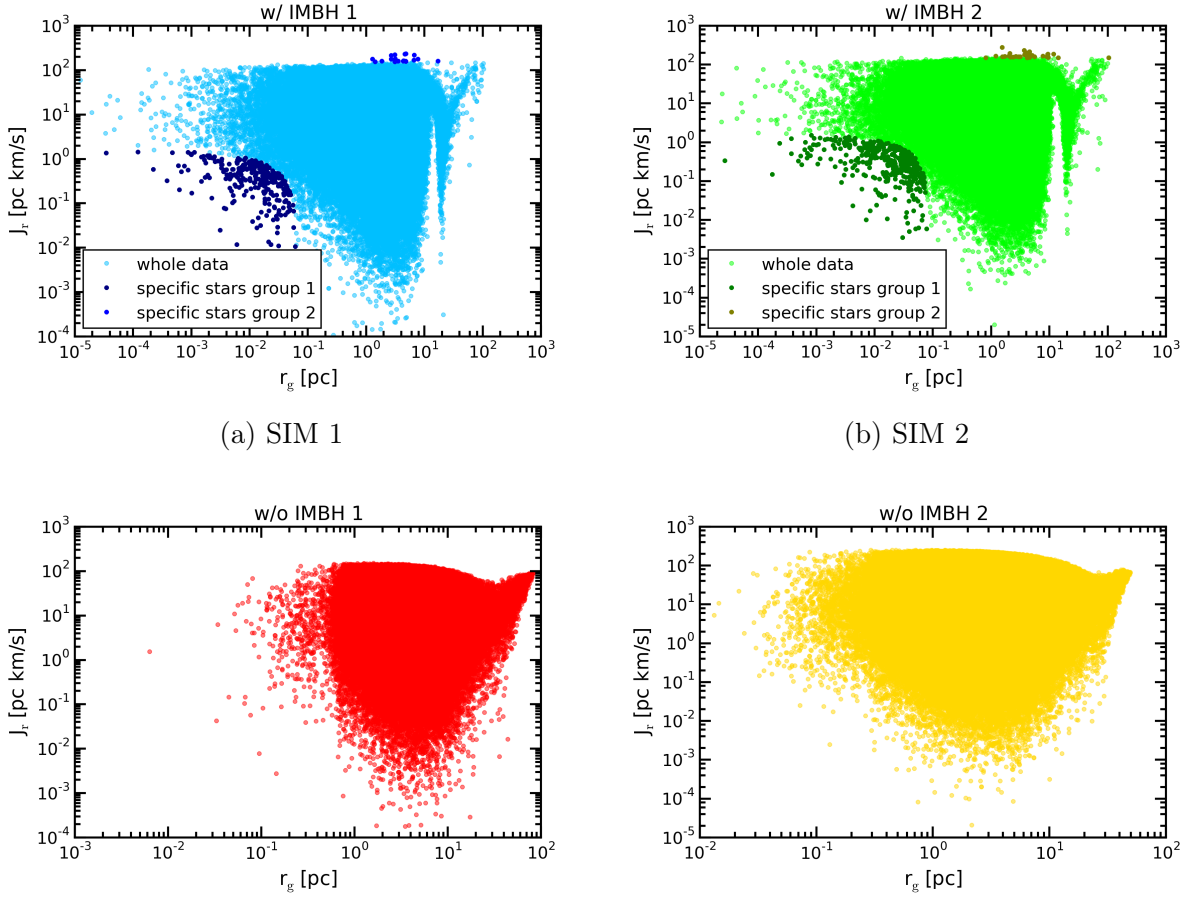

(a) SIM 1

(b) SIM 2

(c) SIM 3

(d) SIM 4

Figure 18: Radial action over guiding star radius with marked specific stars on a double logarithmic scale. All simulations have a similar shaped distributions except for the marked stars which are the specific ones. On the top right corner the shape of a and b is not gently rounded but there are single stars around it. On the lower left there are some extra stars which we identify as the stars with low radial action.

actions are plotted over their guiding star distances. We highlight the stars of group 1 and group 2 taken from graph 13 for SIM 1 and SIM 2. In general, there are several stars which have a really small guiding star radius (up to $10^{-}5\,\mathrm{pc}$). In SIM 3 and SIM 4 only very few stars go below 0.1 pc. Another difference between the GCs with and the ones without IMBH is that on the right border the lower end goes until very low radial

actions for SIM 1 and SIM 2 (up to $10^{-}6\,^{\mathrm{pc\ km}}/_{\mathrm{s}}$) while SIM 3 and SIM 4 end there softly at about $10^{-}2\,^{\mathrm{pc\ km}}/_{\mathrm{s}}$.

4 Results & Discussion

4.1 Signatures of IMBHs in action space

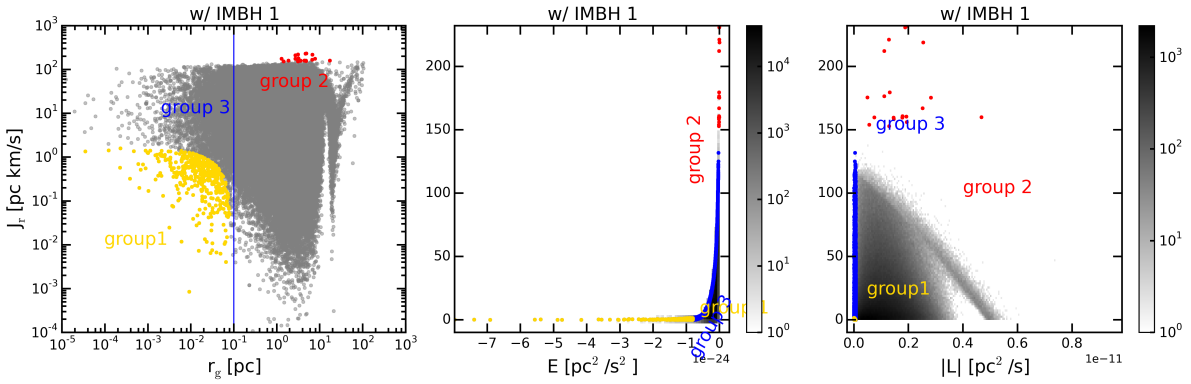

Figure 19: Radial action over different values.

4.2 Discussion & future perspectives

In summary we can say that we found clearly evidence of the IMBH in the radial actions. To get there we made some simplified assumptions which should be investigated more precisely in an extended work.

One of the assumptions regards the density profile. This is at the basis of our action approach because is is necessary to calculate the potential and from that the actions. The density is the basis of our approach of the actions. Since there is not a simple analytical function that can describe the whole profile we interpolated the binned densities and set the central density equal to the innermost density bin. Another attempt to get the density could be done by modelling Multi-Gaussian Expansion to the graph but this goes beyond the goal of our work. We test this procedure changing different values for the central densities. As a result we see that the results for section 4.1 do not change.

Additional inaccuracy of the results rises due to different simulations for GCs with and without IMBH. Since they have different initial conditions and conditions throughout the simulating process we cannot compare them directly. Especially the radial actions can not be compared since they are mass dependent. We see the differences directly in the distributions (figures 4 and 5) and in the anisotropy, possibly due to different truncation prescriptions. In further investigations we should consider using simulations with same conditions despite only the absence of an IMBH in one of the simulations.

Some physical assumptions have been that actions stay totally constant over time or rather that we have only looked at them at the time of the snapshot (despite a few stars for which we integrated the orbit and have looked at the time evolution of their integrals of orbits). Changing integrals of motion go along with changing orbits which could have some numerical fluctuations especially near the IMBH.

Another assumption is that we use specific values if not said else. That means we divide all values by the mass of the stars. We see in fig 16 that there can be distortion due to that. Further work can investigate the mass dependency of the integrals of motion.

If all these points are applied to this method we should think of a way to apply this approach to observational-like data. The main difference is that at this moment there is no possibility to get the masses of the stars of GCs and therefore we can not derive the potential which is essential for this method.

4.3 Test

5 Acronyms

CMD color magnitude diagram

COM centre of mass

DF distribution function

GC globular cluster

HST Hubble Space Telescope

IMBH intermediate mass black hole

MW Milky Way

SMBH super massive black hole

SSP single stellar population

References

Bahcall, J.N. and Wolf, R.A. "Star distribution around a massive black hole in a globular cluster". ApJ, **209**, 214–232, 1976.

Bartelmann, M. "Theoretische Physik I: Punktmechanik und mathematische Methoden". 2008.

Bellini, A., Anderson, J., van der Marel, R.P., Watkins, L.L., King, I.R., Bianchini, P., Chanamé, J., Chandar, R., Cool, A.M., Ferraro, F.R., Ford, H., and Massari, D. "Hubble Space Telescope Proper Motion (HSTPROMO) Catalogs of Galactic Globular Clusters. I. Sample Selection, Data Reduction, and NGC 7078 Results". ApJ, **797**, 115, 2014.

Bianchini, P., Norris, M.A., van de Ven, G., and Schinnerer, E. "Understanding the central kinematics of globular clusters with simulated integrated-light IFU observations". MNRAS, **453**, 365–376, 2015.

Bianchini, P., Varri, A.L., Bertin, G., and Zocchi, A. "Rotating Globular Clusters". ApJ, **772**, 67, 2013.

Binney, J. "Henon's Isochrone Model". *ArXiv e-prints*, 2014.

Binney, J. and Tremaine, S. *Galactic Dynamics: Second Edition.* Princeton University Press, 2008.

Bressan, A., Marigo, P., Girardi, L., Salasnich, B., Dal Cero, C., Rubele, S., and Nanni, A. "PARSEC: stellar tracks and isochrones with the PAdova and TRieste Stellar Evolution Code". MNRAS, **427**, 127–145, 2012.

Carroll, B.W. and Ostlie, D.A. *An introduction to modern astrophysics and cosmology.* 2006.

Downing, J.M.B., Benacquista, M.J., Giersz, M., and Spurzem, R. "Compact binaries in star clusters - I. Black hole binaries inside globular clusters". MNRAS, **407**, 1946–1962, 2010.

Ferrarese, L. and Merritt, D. "A Fundamental Relation between Supermassive Black Holes and Their Host Galaxies". ApJ, **539**, L9–L12, 2000.

Giersz, M. "Monte Carlo simulations of star clusters - I. First Results". MNRAS, **298**, 1239–1248, 1998.

Giersz, M., Leigh, N., Hypki, A., Lützgendorf, N., and Askar, A. "MOCCA code for star cluster simulations - IV. A new scenario for intermediate mass black hole formation in globular clusters". MNRAS, **454**, 3150–3165, 2015.

Harris, W.E. "A Catalog of Parameters for Globular Clusters in the Milky Way". AJ, **112**, 1487, 1996.

Hypki, A. and Giersz, M. "MOCCA code for star cluster simulations - I. Blue stragglers, first results". MNRAS, **429**, 1221–1243, 2013.

Kacharov, N., Bianchini, P., Koch, A., Frank, M.J., Martin, N.F., van de Ven, G., Puzia, T.H., McDonald, I., Johnson, C.I., and Zijlstra, A.A. "A study of rotating globular clusters. The case of the old, metal-poor globular cluster NGC 4372". A&A, **567**, A69, 2014.

Kirsten, F. and Vlemmings, W.H.T. "No evidence for a central IMBH in M 15". A&A, **542**, A44, 2012.

Kroupa, P. "On the variation of the initial mass function". MNRAS, **322**, 231–246, 2001.

Lanzoni, B., Mucciarelli, A., Origlia, L., Bellazzini, M., Ferraro, F.R., Valenti, E., Miocchi, P., Dalessandro, E., Pallanca, C., and Massari, D. "The Velocity Dispersion Profile of NGC 6388 from Resolved-star Spectroscopy: No Evidence of a Central Cusp and New Constraints on the Black Hole Mass". ApJ, **769**, 107, 2013.

Lützgendorf, N., Gebhardt, K., Baumgardt, H., Noyola, E., Neumayer, N., Kissler-Patig, M., and de Zeeuw, T. "Re-evaluation of the central velocity-dispersion profile in NGC 6388". A&A, **581**, A1, 2015.

Lützgendorf, N., Kissler-Patig, M., Gebhardt, K., Baumgardt, H., Noyola, E., de Zeeuw, P.T., Neumayer, N., Jalali, B., and Feldmeier, A. "Limits on intermediate-mass black holes in six Galactic globular clusters with integral-field spectroscopy". A&A, **552**, A49, 2013.

Lützgendorf, N., Kissler-Patig, M., Noyola, E., Jalali, B., de Zeeuw, P.T., Gebhardt, K., and Baumgardt, H. "Kinematic signature of an intermediate-mass black hole in the globular cluster NGC 6388". A&A, **533**, A36, 2011.

Maccarone, T.J. and Servillat, M. "Radio observations of NGC 2808 and other globular clusters: constraints on intermediate-mass black holes". MNRAS, **389**, 379–384, 2008.

Meylan, G. and Heggie, D.C. "Internal dynamics of globular clusters". A&A Rev., **8**, 1–143, 1997.

Miller, M.C. and Hamilton, D.P. "Production of intermediate-mass black holes in globular clusters". MNRAS, **330**, 232–240, 2002.

Mohr, P.J., Newell, D.B., and Taylor, B.N. "CODATA Recommended Values of the Fundamental Physical Constants: 2014". *ArXiv e-prints*, 2015.

Noyola, E., Gebhardt, K., and Bergmann, M. "Gemini and Hubble Space Telescope Evidence for an Intermediate-Mass Black Hole in ω Centauri". ApJ, **676**, 1008-1015, 2008.

Piotto, G., Milone, A.P., Bedin, L.R., Anderson, J., King, I.R., Marino, A.F., Nardiello, D., Aparicio, A., Barbuy, B., Bellini, A., Brown, T.M., Cassisi, S., Cool, A.M., Cunial, A., Dalessandro, E., D'Antona, F., Ferraro, F.R., Hidalgo, S., Lanzoni, B., Monelli, M., Ortolani, S., Renzini, A., Salaris, M., Sarajedini, A., van der Marel, R.P., Vesperini, E., and Zoccali, M. "The Hubble Space Telescope UV Legacy Survey of Galactic Globular Clusters. I. Overview of the Project and Detection of Multiple Stellar Populations". AJ, **149**, 91, 2015.

Plummer, H.C. "On the problem of distribution in globular star clusters". MNRAS, **71**, 460–470, 1911.

Rubin, V.C., Ford, W.K.J., and . Thonnard, N. "Rotational properties of 21 SC galaxies with a large range of luminosities and radii, from NGC 4605 /R = 4kpc/ to UGC 2885 /R = 122 kpc/". ApJ, **238**, 471–487, 1980.

Strader, J., Chomiuk, L., Maccarone, T.J., Miller-Jones, J.C.A., Seth, A.C., Heinke, C.O., and Sivakoff, G.R. "No Evidence for Intermediate-mass Black Holes in Globular Clusters: Strong Constraints from the JVLA". ApJ, **750**, L27, 2012.

van der Marel, R.P. and Anderson, J. "New Limits on an Intermediate-Mass Black Hole in Omega Centauri. II. Dynamical Models". ApJ, **710**, 1063–1088, 2010.

Zocchi, A., Bertin, G., and Varri, A.L. "A dynamical study of Galactic globular clusters under different relaxation conditions". A&A, **539**, A65, 2012.